GFZ
Helmholtz-Zentrum
POTSDAM

Originally published as:

Eken, T., Plomerova, J., Vecsey, L., Babuska, V., Roberts, R., Shomali, H., Bodvarsson, R. (2012): Effects of seismic anisotropy on P-velocity tomography of the Baltic Shield. - Geophysical Journal International, 188, 2, pp. 600—612.

DOI: http://doi.org/10.1111/j.1365-246X.2011.05280.x

Geophysical Journal International

Geophys. J. Int. (2012) **188,** 600–612 doi: 10.1111/j.1365-246X.2011.05280.x

Effects of seismic anisotropy on P-velocity tomography of the Baltic Shield

Tuna Eken,[1,2*] Jaroslava Plomerová,[2] Luděk Vecsey,[2] Vladislav Babuška,[2] Roland Roberts,[1] Hossein Shomali[1] and R. Bodvarsson[1]

[1] *Department of Earth Sciences, Uppsala University, Geophysics, Villavägen* 16, 75236 Uppsala, *Sweden. E-mail: Tuna.Eken@gmail.com*
[2] *Geophysical Institute, Czech Academy of Science,* 141 31 *Praha* 4, *Czech Republic*

Accepted 2011 October 21. Received 2011 October 10; in original form 2010 June 30

ABSTRACT

We investigate possible effects of neglecting seismic anisotropy on standard isotropic *P*-velocity tomographic images of the upper mantle beneath the Baltic shield. Isotropic inversions of teleseismic *P*- and *S*-wave traveltimes exhibit alternating high- and low-velocity heterogeneities down to depths of over 400 km. Differences in tomographic inversions of *SV*- and *SH*-wave traveltimes are distinct down to depths of about 200 km and are associated with anisotropy of the lithospheric mantle. Anisotropic structures of the upper mantle affect both the *P* and *S* traveltimes, shear-wave splitting as well as the *P* polarization directions. Joint inversion for isotropic and anisotropic velocity perturbations is not feasible due to the limited 3-D ray coverage of available data. Therefore, we correct the input traveltimes for anisotropic contributions derived from independent analyses and then perform standard isotropic inversions. These corrections are derived either directly from directional deviations of *P*-wave propagation or are calculated in anisotropic models retrieved by joint inversions of body-wave anisotropic parameters (*P*-residual spheres and shear-wave splitting). These anisotropic models are also used to fit backazimuth variations of *P*-wave polarization directions. General features of tomographic images calculated from the original and the anisotropy-corrected data are similar. Amplitudes of the velocity perturbations decrease below ∼200 km depth, that is in the sub-lithospheric mantle. In general, large-scale anisotropy related to the fabrics of the continental mantle lithosphere can contaminate tomographic images in some parts of models and should not be ignored.

Key words: Body waves; Seismic anisotropy; Seismic tomography; Cratons.

1 INTRODUCTION

Seismic tomography is an important tool in imaging the 3-D velocity structure of the deep Earth. For an overview of the current state of the art in seismic tomography we refer to Rawlinson *et al.* (2010). In general, such tomography uses traveltimes or waveforms recorded by a local, regional or global seismic network. Tomographic methods depend on an array configuration and a depth of modelled volume (e.g. Thurber & Ritsema 2007). Studies of the upper mantle structure exploit teleseismic signals recorded by large and dense arrays of temporary stations (e.g. Aki & Lee 1976; Aki *et al.* 1977; Evans & Achauer 1993, for a review). The most common tomographic approach is to invert traveltimes of seismic waves to estimate velocities, or velocity perturbations within the Earth, though it is possible to invert for other parameters, for example for the attenuation in different zones of the Earth. Results of the inversions are used to constrain structure of the mantle, temperature and composition, and to contribute to our understanding of the geodynamic history of individual tectonic provinces.

Standard body-wave tomographic studies invert the traveltime delays (deviations between observed traveltimes and those modelled using an initial Earth model) under the assumption that the Earth is isotropic. However, Earth forming rocks are anisotropic and the Earth's structure, especially in the upper few hundreds of kilometres, has been proved to be anisotropic on a large scale. Relevant data is provided by the well-established SKS splitting techniques (Ando *et al.* 1983; Vinnik *et al.* 1984; Silver & Chan 1988; Šílený & Plomerová 1996; Savage 1999; Levin *et al.* 1999; Fouch & Rondenay 2006), directional variations of *P*-wave traveltime delays (Babuška *et al.* 1984; Babuška & Plomerová 2006; Plomerová *et al.* 1996; Hearn 1996; Eberhart-Phillips & Henderson 2004; Hirahara & Ishikawa 1984; Ishise & Oda 2008) and dispersion of Love and Rayleigh waves (e.g. Anderson 1961; Aki & Kaminuma 1963; Anderson & Dziewonski 1982; Montagner

*Now at: GFZ, Potsdam,Telegrafenberg, D 409 D-14473 Potsdam, Germany

© 2011 The Authors
Geophysical Journal International © 2011 RAS

1998; Bruneton *et al.* 2004). Recent methods of evaluating converted waves (e.g. Levin *et al.* 2008) provide additional constrains on the anisotropic structure. Laboratory measurements of mantle xenoliths reveal significant mantle anisotropy (Mainprice & Silver 1993; Ben-Ismail & Mainprice 1998). While seismic anisotropy within the crust reflects layering of sediments, oriented cracks of variable length and width or foliation of rock complexes, the large-scale anisotropy in the mantle is generally associated with lattice preferred orientation (LPO) of olivinic rocks (Babuška & Cara 1991).

Seismic anisotropy affects traveltimes, implying that it might distort tomographic images retrieved under the assumption of isotropic structure. Inverting the traveltime deviations for velocity in anisotropic models has been attempted (e.g. Grésillaud & Cara 1996), but it is difficult mainly due to limited ray-coverage in relation to this complex 3-D task. However, with the use of *a priori* knowledge about the structure, particularly in defining regions with similar anisotropy in the upper mantle, information on the fabric of mantle lithosphere can be retrieved independently. Grésillaud & Cara (1996) reported that anisotropy has a small influence if it is laterally homogeneous over the scale of the seismic array but the effect of laterally heterogeneous anisotropy on isotropic tomography images beneath the receiver array may be more significant. Sobolev *et al.* (1999) showed that seismic anisotropy affects isotropic tomographic images and that these effects depend both on the strength of anisotropy and on ray-coverage. They suggested that possible artifacts introduced by anisotropy may be largest for regions where a fossil subduction zone with dipping olivine *a* axis exists. Lloyd & van der Lee (2008) analysed shear and surface Rayleigh waves using waveform inversion and reported that azimuthal anisotropy can cause a small bias in the final images of Earth structure.

Previous analyses of *P*-wave traveltimes and shear-wave splitting directionality indicate that the Precambrian mantle lithosphere of Fennoscandia can be mostly modelled by dipping foliations in the Proterozoic part and a plunging lineation in the Archean part (Plomerová *et al.* 2001, 2006, 2008; Vecsey *et al.* 2007; Eken *et al.* 2010). Discrepancies between isotropic inversions of radial and tangential components (SV and SH) of direct shear waves at depths down to ∼150–200 km, which are depths corresponding to an estimate of the lithosphere–asthenosphere boundary (LAB, Plomerová *et al.* 2008; Plomerová & Babuška 2010), have been attributed to the effect of large-scale anisotropy in the mantle lithosphere (Eken *et al.* 2008, 2010).

This paper aims at evaluating effects due to neglecting anisotropy in isotropic velocity images by comparing the upper mantle velocity images calculated with and without considering seismic anisotropy. For this purpose, we extract information regarding anisotropy within the upper mantle from Eken *et al.* (2010), where we modelled fabrics of individual mantle lithosphere domains of the Baltic Shield by joint inversion of shear-wave splitting and *P*-wave traveltime residuals evaluated from recordings of the Swedish National Seismological Network (SNSN). We apply two types of corrections for anisotropy to the traveltime residuals associated with individual rays used in the isotropic velocity tomography. The aim of the corrections is to minimize effects of anisotropy in data before the inversion for isotropic velocity perturbations is performed, because there is currently no tool to invert robustly our traveltimes both for anisotropy and heterogeneity simultaneously. In addition, we evaluate the *P*-wave polarization (P_{pol}) to test the anisotropic models of the mantle lithosphere derived from both the *P* and *S* waves.

2 DATA

We analyse traveltimes of *P*-waves recorded at 45 stations of the Swedish National Seismic Network (SNSN, Fig. 1) operated by Uppsala University since 1998 (see Bödvarsson 1999; Olsson 2007 and Eken *et al.* 2007, 2008 for more details). Inter-station spacing of the SNSN varies from 30 to 100 km with an average of 70 km. The data consists of about 4200 *P*-wave arrival times picked manually on the high pass (WWSSN 1Hz, Oliver and Murphy 1971) filtered broad-band recordings of 136 teleseismic earthquakes from epicentral distances between 30° and 90°, and with magnitudes of at least 5.5 (Fig. 2).

We assigned a quality factor to each measured arrival time for its weighting in the later analysis according to estimated picking accuracy, ranging between 0.05 and 0.3s. Events used in the tomographic inversions of Eken *et al.* (2007, 2008) form a core of the data set. For improved ray coverage these data are complemented with more recent events and events not previously used because their back-azimuths were not well-suited to the earlier analyses (Eken *et al.* 2010). The enhanced data set particularly improves resolution in the northern part of the array, where some stations were only recently installed.

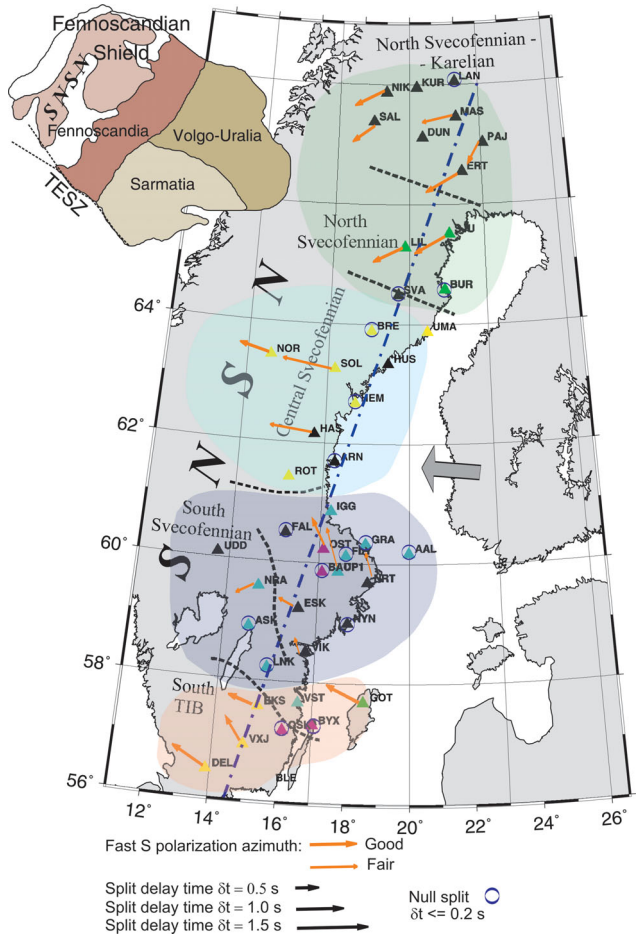

Figure 1. Stations of the Swedish National Seismic Network (SNSN) coloured according to their *P*-residual sphere pattern (Eken *et al.* 2010; see also Fig. 3) along with location of a profile shown in Fig. 8. Arrows demonstrate geographical variations of the shear-wave splitting parameters evaluated for an event. Coloured provinces mark four main domains of similar fabrics within the mantle lithosphere according to body-wave anisotropy (Eken *et al.* 2010).

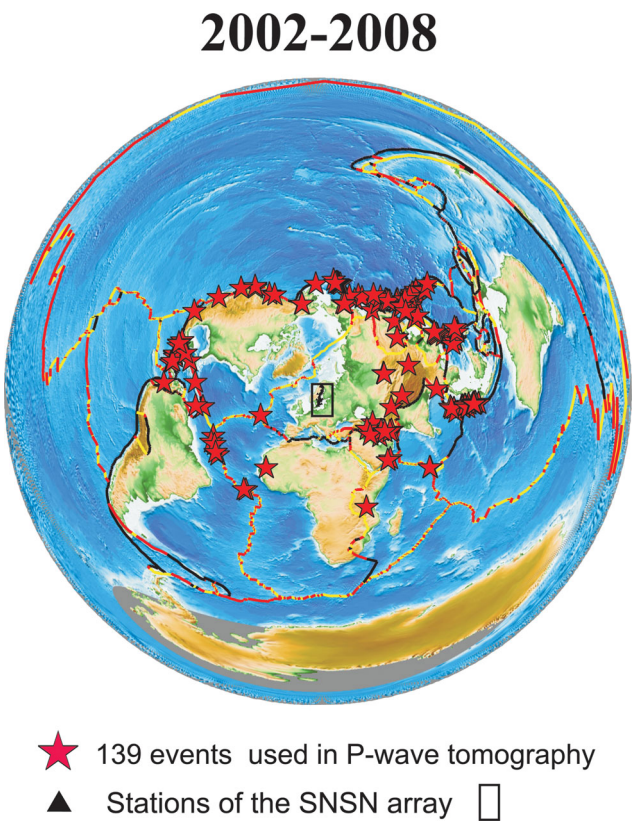

Figure 2. Distribution of 136 teleseismic earthquakes occurred during 2002 – 2008 and used in the study. Plate boundaries are after Bird (2003).

3 METHODS

3.1 3D inversion for isotropic velocity perturbations of the upper mantle

The traveltime t of a seismic wave through a medium along a path s can be described (Nolet 1987; Thurber & Ritsema 2007) by

$$t_i = \int_{s_i} \frac{\mathrm{d}s_i}{v(r)} \tag{1}$$

where index i stands for the ith ray and v is the seismic velocity of the medium at point r, which is a scalar describing the distance along the ray path. Because both the traveltime t and path s are functions of velocity v, estimation of velocity via inversion of traveltimes for many rays is in general a non-linear problem. However, assuming that the velocity perturbations are small on the large scale, laterally homogeneous isotropic radial Earth models for example IASP91 (Kennett and Engdahl 1991) provide a good approximation of teleseismic ray paths. For each ray, the traveltime to each station from each earthquake focus is calculated assuming the reference Earth model. This is subtracted from the observed traveltime, providing our traveltime residuals δt_i for inversion. In large-scale studies, with teleseismic foci lying outside the analysed volume, we have to suppress effects of possible source mislocation and velocity perturbations outside the volume for which we invert. This is achieved by subtracting an event traveltime mean residual (over the recording array) and then by inverting relative residuals. Differences between the observed traveltimes and the traveltimes calculated for a reference radial Earth model (traveltime residuals) can be approximated by

$$\delta t_i = -\iint_{s_0} \frac{\delta_v(r)}{\delta_0^2(r)} \mathrm{d}s \tag{2}$$

where $\delta v(r)$ represents velocity perturbations relative to a laterally homogeneous model with velocity v_0 and s_0 the ray path in this model. This assumes the velocity perturbations are small and do not deviate substantially the rays from the unperturbed ray paths within the reference model. By assuming that the Earth is built up of constant velocity cells, eq. (2) can be written as a system of linear equations and be inverted for the unknown model parameters (Nolet 1987),

$$d = Ax \tag{3}$$

where d is the data vector of length N and x is the model parameter vector of length M, where M is the number of unknown cell velocities in the model. The matrix A is known as Frechet matrix and represents the matrix of the partial derivatives of the data with respect to the model parameters.

A linearized ACH approach (Aki *et al.* 1977; Evans & Achauer 1993) was repeatedly applied during the inversions. The method is the back-projection of relative traveltime residuals to estimate the magnitude and spatial distributions of velocity perturbations within a heterogeneous volume beneath the receiver area. There are several inversion methods (Menke 1989) to solve the linearized systems (3) and we used a weighted damped least squares approach,

$$x^{\mathrm{est}} = [A^T W^{\mathrm{d}} A + \varepsilon^2 W^x]^{-1} A W^{\mathrm{d}} d \tag{4}$$

where x^{est} defines the model vector including velocity perturbations. In eq. (4), W^{d} indicates the data error. It is determined during the data picking. W^x stands for a smoothing operator and corresponds to model roughness. For discrete model parameters either the difference between physically adjacent model parameters as an approximation of solution roughness or alternatively the second derivative of traveltime with respect to model parameters can be used. ε^2 is the damping factor that ensures the stability of the inversion. W^{d} and ε^2 need to be defined *a priori* to the inversion (i.e. Nolet 1987; Menke 1989; Thurber & Ritsema 2007).

To quantify success in modelling the upper mantle structures we calculate the variance reduction

$$\text{variance reduction} = \left(1 - \frac{\sum_{i=1}^{N}(d_{\mathrm{obs}(i)} - \hat{d_{\mathrm{obs}}})^2}{\sum_{i=1}^{N}(d_{\mathrm{est}(i)} - \hat{d_{\mathrm{est}}})^2}\right) \cdot 100 \tag{5}$$

where d_{obs} and d_{est} are observed data and estimated data (after the 4th iteration) vectors, respectively, and both $\hat{d_{\mathrm{obs}}}$ and $\hat{d_{\mathrm{est}}}$ represent their corresponding mean. The variance reduction is calculated for each type of inversion and data independently.

3.2 Elimination of anisotropy

If traveltimes are perturbed by anisotropy, eq. (3) can be re-written as follows (Lloyd & van der Lee 2008),

$$d = A(x_{\mathrm{iso}} + x_{\mathrm{aniso}} + x_{\mathrm{bias}}) = d_{\mathrm{iso}} + d_{\mathrm{aniso}} + d_{\mathrm{bias}} \tag{6}$$

The observed data vector d is assumed to consist of three parts: d_{iso} which represents isotropic deviations of velocity from a reference model: d_{aniso} which describes contributions due to anisotropy, and a residual term d_{bias} which reflects small-scale heterogeneities and noise. Given the anisotropic component of the

traveltime perturbation ($d_{\rm aniso}$) then this component can be removed and the data then inverted for $d_{\rm iso}$ assuming an isotropic medium. If we can reliably identify $d_{\rm aniso}$ this should provide more reliable tomographic images with the bias due to anisotropy removed.

We use two independent methods to estimate and then to minimize the effects of anisotropy in our isotropic inversions. We exploit inferences from the *P*-wave residual analysis and shear wave splitting (Eken *et al.* 2010) to estimate the bulk anisotropic character of different domains beneath the SNSN array assuming that anisotropy within each domain is fairly consistent (in direction and magnitude) on a large scale. This information is then used to correct traveltime for each individual ray.

To estimate the anisotropy data vector, $d_{\rm aniso}$ we initially used the technique proposed in its original form in Babuška *et al.* (1984) and later modified in Babuška & Plomerová (1992). The updated procedure allows us to homogenize the azimuth–incidence angle coverage of the volume studied by station (i)–event (j) rays automatically clustered into azimuth–epicentral distance (or incidence angle) bins (k) and to calculate automatically two isotropic terms—the static term $R_i^{\rm st}$ and directional mean $R_i^{v\_{\rm iso}}$ at the ith station. The static term is calculated from steeply incident rays and is used for estimates of lateral variations in the LAB depth, while the directional mean calculated as an average relative residual from all directions, serves as an estimate of isotropic velocity beneath the station. Depending upon the number of events processed and their spatial distribution it may be appropriate to work with bin-allocated residuals $R_{i,k}$ in bins of for example 20°(azimuth)-by-10°(epicentral distance). Alternatively, we can evaluate traveltime deviations $R_{i,j}$ at stations for 'single events' (j) individually. The latter approach was used to retrieve corrections for anisotropy of the SNSN data (traveltimes) for tomography, in order to be able to correct times for individual rays.

The single station directional terms $R_{i,j}^{\rm anis}$, are deviations of the relative residuals $R_{i,j}$ from the directional mean $R_i^{v\_{\rm iso}}$. We used the most frequently used procedure to calculate relative residuals for a teleseismic event by subtracting a normalizing value represented by a mean of traveltimes of all stations which recorded the jth event. A general pattern of *P* spheres showing the directional terms $R_{i,j}^{\rm anis}$, can be associated mainly with the effects of large-scale anisotropy, although they contain effects of small-scale heterogeneities, located particularly in the crust. Our first type of data correction for anisotropy—the A type—is based purely on the *P*-wave analysis. We subtract the directional terms $R_{i,k}^{\rm anis}$ (where k stands for each individual event) from the traveltime of each ray. Our second type of correction for anisotropy—the B type—is based on the anisotropic models of individual domains (blocks) of mantle lithosphere retrieved in Eken *et al.* (2010) by joint inversion of body-wave anisotropic parameters. The mantle lithosphere beneath the SNSN consists of sharply bounded anisotropic blocks of apparently uniform fabrics approximated by hexagonal symmetries with either dipping high velocity (a,c) foliations (the b-axis models) or plunging lineation a (the a-axis models; Plomerová & Babuška 2010). We calculate the anisotropy contribution to each ray by shooting through the 3-D anisotropic models retrieved by joint inversion of both the *P*-wave residuals ($R_{i,k}$) and shear-wave splitting data (Šílený & Plomerová 1996; Eken *et al.* 2010) separately for each anisotropic domain of the mantle lithosphere. Anisotropic signals at stations above boundaries of domains with different fabric often disappear ('no P pattern,' null splitting; Babuška & Plomerová 2006) and we do not apply any corrections on traveltimes recorded at such stations. For five selected stations, Fig. 3 shows examples of observed directional terms of relative residuals plotted for each individual ray as well as synthetics, representing the A- and B-type corrections, respectively.

3.3 *P* polarizations ($P_{\rm pol}$)

In homogeneous isotropic media, the *P*-wave particle motion is restricted to the ray direction. This means that the radial component of the particle motion observed at the surface of such a medium is linear and parallel to the backazimuth (φ). Any deviation of the observed horizontal polarization direction ($P_{\rm pol}$) of long period *P*-waves from the radial direction and its dependence on the event backazimuth can be due to: (i) sensor misorientation, (ii) dipping structures, (iii) seismic anisotropy, and (iv) velocity heterogeneities beneath the receiver (Schulte-Pelkum *et al.* 2001; Fontaine *et al.* 2009). Variations of the observed deviations ($\delta\varphi$) of the $P_{\rm pol}$ in dependence on backazimuth can be fit by a harmonic function:

$$\delta\varphi = A_1 + A_2\sin(\varphi) + A_3\cos(\varphi) + A_4\sin(2\varphi) + A_5\cos(2\varphi) \qquad (7)$$

where A_1 is a constant related to sensor misorientation, A_2 and A_3 indicate dipping structures (e.g. dipping interface, or dipping anisotropic structure) and A_4 and A_5 characterize effects of anisotropy with horizontal symmetry axes. Pairs A_2, A_3 and A_4, A_5 differ in rotational symmetry. A_2 and A_3 have 2π periodicity while A_4 and A_5 have π periodicity.

A comparison between these two pairs, defined as

$$\delta{\rm dip}_{\rm max} = \sqrt{A_2^2 + A_3^2} \quad \delta\eta_{\rm max} = \sqrt{A_4^2 + A_5^2} \qquad (8)$$

gives a measure of the predominance of either effects of dipping structures, if $\delta{\rm dip}_{\rm max} > \delta\eta_{\rm max}$ (including anisotropy with dipping symmetry axis), or effects of azimuthal anisotropy, that is anisotropy with horizontal symmetry axis if $\delta\eta_{\rm max} > \delta{\rm dip}_{\rm max}$ (Fontaine *et al.* 2009).

Following the procedure of Fontaine *et al.* (2009) and using recordings of earthquakes from epicentral distances of 10°–70°, we filtered the broad-band data with a 14–33 s bandpass Butterworth filter. We selected recordings at two stations, below which we retrieved different fabrics in the mantle lithosphere approximated by different symmetries (Eken *et al.* 2010), and tried to model the observed $P_{\rm pol}$ dependences on backazimuth. We detected $P_{\rm pol}$ deviations at 123 out of 419 and 94 out of 423 high-quality recordings at stations HEM and SJU, respectively (see Figs 1 and 3). To calculate synthetics for different models we used the 'Raysum' code of Frederiksen and Bostock (2000).

4 MANTLE LITHOSPHERE ANISOTROPY BENEATH THE SNSN

We have shown (Eken *et al.* 2010) that the mantle lithosphere beneath the SNSN consists of sharply bounded anisotropic domains, whose fabric we model by hexagonal symmetries with dipping high-velocity (a,c) foliations (the b-models) or plunging lineation a (the a-models; Plomerová & Babuška 2010). Both the *P* traveltime delays and shear-wave splitting at individual stations show systematic variations. Importantly, the variations observed at neighbouring stations are often very similar. We grouped stations with similar pattern (see Fig. 1 SNSN-stations) into five large groups and delimited domains of mantle lithosphere with homogenous fabric, separated by distinct boundaries.

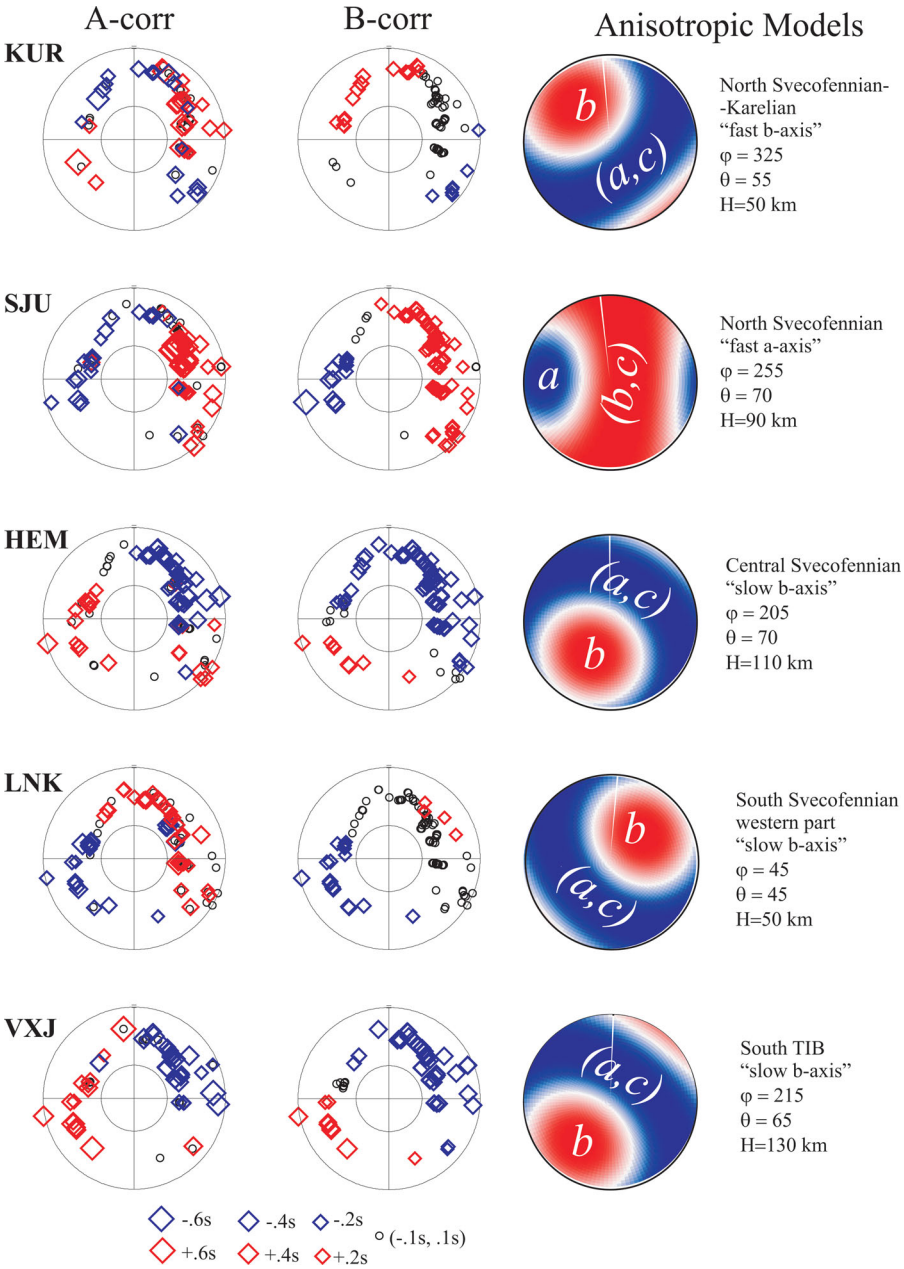

Figure 3. Examples of directional terms of relative *P*-wave residuals plotted for each individual ray at five selected stations. The observed values represent the A-type corrections for anisotropy (left-hand column). Synthetic values (central column), the B-type corrections, were calculated for the 3-D self-consistent anisotropic models (right-hand column) retrieved by the joint inversions of body-wave anisotropic parameters. The models represent fabrics of individual mantle lithosphere domains bellow the SNSN (Eken *et al.* 2010).

Amplitudes of the directional terms of relative *P* residuals shown in the *P* spheres (see examples in Fig. 3) are usually between −0.5 s and +0.5 s and their distributions exhibit the so-called bipolar pattern at most of the stations. Only anisotropic models with plunging symmetry axes are consistent with the characteristic patterns of the spheres, that is negative terms—earlier arrival, relatively fast directions of propagation—observed in one half of the lower hemisphere projection and positive terms—delayed arrivals, relatively slow directions of propagation—in the opposite side of the hemisphere. For each group we show (Fig. 3) the *P*-sphere pattern at one of the stations (the directional terms of relative residuals for each single ray) used in the joint inversion with the shear-wave splitting parameters (the fast *S* polarizations and split delay times). The retrieved 3-D self-consistent anisotropic models (Eken *et al.* 2010) are shown as well, along with synthetic estimates of the anisotropic contribution to the *P*-wave propagation calculated for the individual models at the selected stations. The observed residual terms in the left-hand column represent the A-type correction (A-corr), the synthetic terms in the middle column, calculated for the anisotropic models, represent the B-type correction (B-corr) of the original traveltimes. Traveltimes at stations with 'no P pattern' were not corrected.

The synthetic *P* spheres calculated for the anisotropic models are smoother compared with the observed spheres, where small-scale heterogeneities may be observed, for example the isolated negative residual terms for steep rays with backazimuths ∼45°

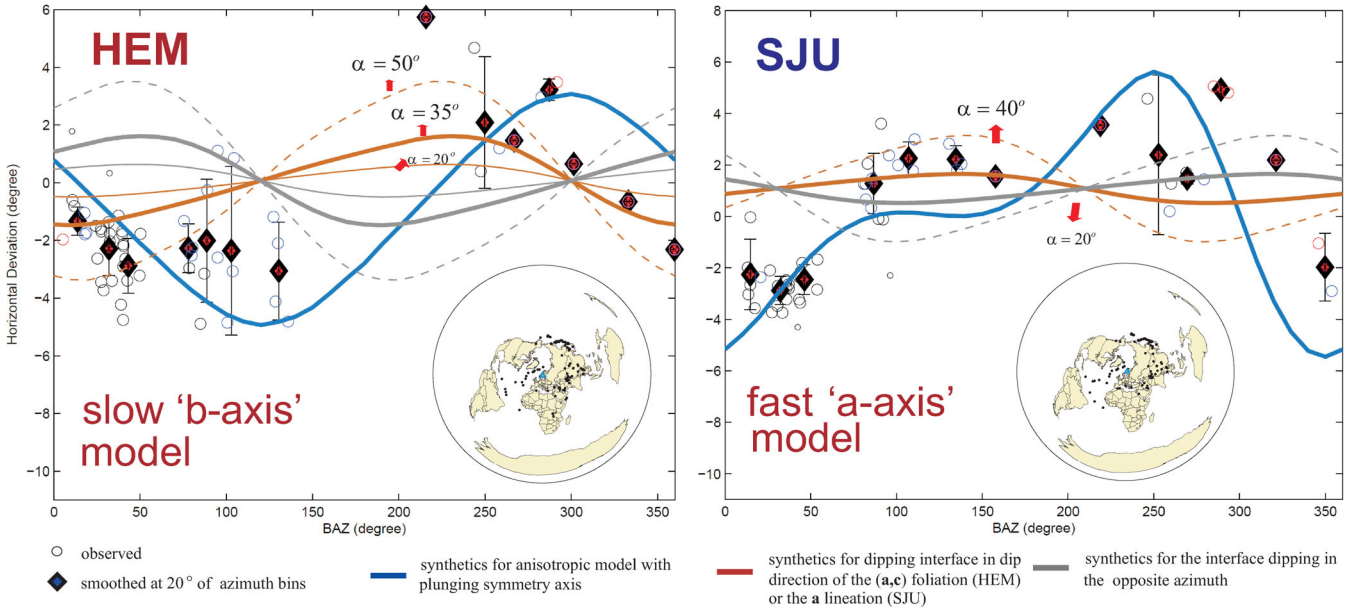

Figure 4. Variations of *P*-wave polarizations (P_{pol}) with backazimuth for two stations representing two lithosphere domains, whose anisotropy is modelled (Fig. 3) with different symmetries. In both cases, the anisotropic models better explain the azimuthal variations of the observed horizontal deviations of polarizations than the isotropic models with dipping interfaces. All together, 123 and 94 regional/teleseismic earthquakes were used to measure P_{pol} at stations HEM and SJU, respectively.

at station LNK. However, in general there is a good agreement between the A-corr and B-corr spheres for stations in the South Trans-Scandinavian Igneous Belt (TIB), and the Central and North Svecofennian region (VXJ, HEM and SJU). The South Svecofennian and the North Svecofennian–Karelian regions have more complex structure. The South Svecofennain region, here represented by an anisotropic model of its western part (Fig. 3), seems to consist of several smaller fragments, which differently affect the short-period *P* waves. However, the cumulative character of the P data and also the broad-band *S* data do appear to show consistent patterns related to larger scale structure. The observed *P* pattern in the northernmost region, around the Svecofennian–Karelian transition, differs from the general bipolar pattern, and thus the model retrieved by the joint inversion does not mimic the observed pattern satisfactorily.

There are distinct dependencies of P_{pol} on backazimuths for the two stations shown in Fig. 4, selected in different tectonic environments. Station SJU is located in the Northern Svecofennian, where mantle lithosphere fabric is approximated by the 'fast' *a*-axis model with westward dipping high-velocity lineation *a*. Inclination angle of the fast *a* axis 'a' is 20° from the horizontal. Station HEM is situated in the Central Svecofennian and the underlying mantle lithosphere is modeled by 'slow' *b*-axis hexagonal symmetry with the high-velocity (a,c) foliation dipping to the NE at 35° from the horizontal (Eken *et al.* 2010). Though there is a gap in the backazimuth coverage for station HEM compared with station SJU, the 2π-periodicity is evident in both graphs. $\delta \mathrm{dip}_{max}$ is larger than $\delta\eta_{max}$ for both stations (Table 1) indicating thus a presence of dipping structures, that is either dipping interfaces between two isotropic velocities or anisotropic structures with dipping symmetry axes. To fit the P_{pol} variations we calculated synthetics for both dipping interfaces and the anisotropic models as retrieved by the joint inversion of body-wave anisotropic parameters (Šílený & Plomerová 1996). While the synthetics for the anisotropic models fit the variations well for almost all the azimuth ranges, the dipping interfaces do not. Furthermore, we were unable to find a dipping interface structure which we considered realistic and which could generate the observed magnitude of azimuth deviations.

Table 1. Coefficients of the P_{pol} variations calculated after the harmonic analysis.

Station	HEM	SJU
A_1	0.0707 ± 0.23653	1.0852 ± 0.21042
A_2	-2.6974 ± 0.24791	-1.2992 ± 0.27898
A_3	-1.8259 ± 0.3855	-1.7876 ± 0.32624
A_4	0.8698 ± 0.28876	-1.1424 ± 0.29031
A_5	0.1682 ± 0.324	-1.1452 ± 0.30884
$\delta \mathrm{dip}_{max}$	3.2573	2.2099
$\delta\eta_{max}$	0.8859	1.6176

5 TOMOGRAPHIC INVERSIONS WITH CORRECTIONS FOR ANISOTROPY

To search for effects of upper mantle seismic anisotropy in images retrieved by the isotropic inversions we present the velocity perturbations at individual nodes (Fig. 5). At least 20 rays per node were set as a minimum to consider a node as resolved. A 3-D crustal model derived from Korsman *et al.* (1999) is used to correct the travel times for the Fennoscandian crust relative to the reference model (IASP91). The model volume is parameterized by 9-by-17 nodes in horizontal plane (plus two in each direction to stabilize the inversion) and by 17 nodes in the vertical direction. To ensure the stability of the inversion, a damping parameter of 100 $s^2\%^{-2}$ was employed in the inversions of uncorrected and the A- and B-type corrected data (eq. 4). The optimal damping parameter was assessed by conducting a set of inversions with a broad interval of damping values (5 and 1000 $s^2\%^{-2}$) and from trade-off curves between data variance and model length (normalized squared summation of the model perturbations, Eken *et al.* 2007). For clarity in comparing the traditional isotropic inversion with that after application of the innovative method of data preprocessing we have used the same

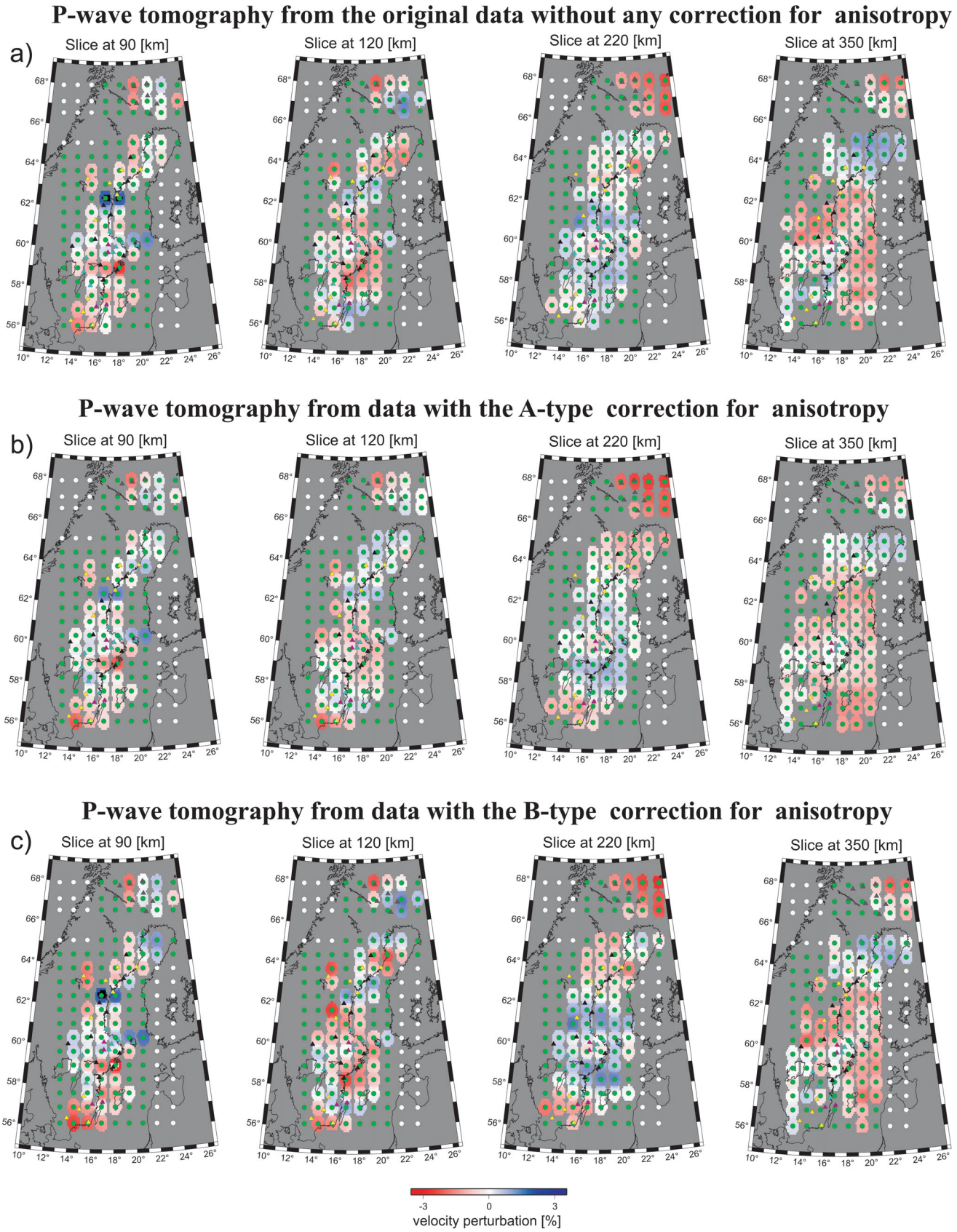

Figure 5. Example model velocities from the horizontal slices of nodes at depths of 90, 120, 220 and 350 km (a) Velocity perturbations retrieved from isotropic tomography calculated from the original data, that is with no correction for anisotropy. (b) Velocity perturbations from isotropic tomography using data with the A-type correction for anisotropy, based purely on the directional terms of the relative *P*-residual. (c) As *b* but using data with the B-type correction for anisotropy, based on synthetic contributions due to anisotropy calculated for the 3-D self-consistent anisotropic models (see Fig. 3).

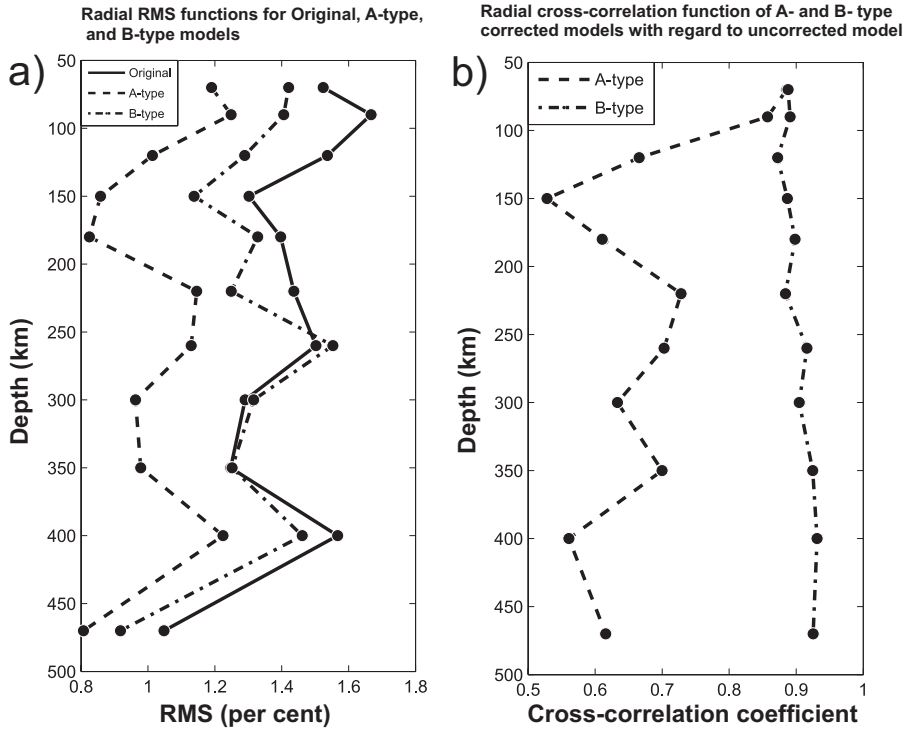

Figure 6. Radial rms functions (a) of resulting velocity models calculated from original data and data with the A-type and B-type corrections for anisotropy. Cross-correlation functions (b) between the models calculated from original and anisotropy corrected data.

damping factor throughout. The dependency of the variance reduction on the damping factor is similar for the different inversions and the curves differ in absolute values only (Fig. 7).

Variance reductions of the final models range from 51 to 79 per cent. The largest reduction is for the A-type corrected data implying that this model better fits the data under the same model parameterization conditions (i.e. horizontal and vertical grid spacing, initial 1-D reference model, damping, etc.). The velocity perturbations with damping factor of 100 are shown at slices of nodes at example depths of 90, 120, 220 and 350 km (Fig. 5).

Although, only small differences between the images from the different inversions are observed, a thorough comparison of the three models requires a quantitative statistical analysis. Therefore, we calculated radial root mean square (rms) and cross-correlation functions of the estimated velocity perturbations to evaluate the differences at each layer. The rms of velocity perturbations, shown as a function of depth (Fig. 6a), range from ∼0.8 to 1.7 per cent. As we would expect, the original and the B-type corrected models are closer to each other, than they are to the A-type corrected model. This reflects the fact that the A-type corrections reduce the effects of anisotropy, but the corrections also include noise (in a broader sense). Moreover, for the A-type correction, all rays at all stations could be corrected. On the other hand, the B-type correction reduces only the effects of anisotropy according to the 3-D models of the mantle lithosphere retrieved by the joint inversion of independently evaluated anisotropic parameters. However, we could only correct rays propagating within one anisotropic domain, thus leaving data at stations around the domain boundaries uncorrected. Specifically, only residuals at 2/3 of all stations, that is 31 out of 45 stations, could be corrected. But waves propagating to the remaining stations are influenced by the mantle anisotropy as well. The shapes of the depth-dependencies of the rms curves for all three models are similar, particularly in the mantle at depths below ∼250 km. Cross-correlation coefficients around 0.9 calculated for the B-type models with respect to the original model (Fig. 6b) stress the strong similarity between the models. Correlation between the A-type model and the model from uncorrected data is lower. These findings are not surprising, because the A-type correction cleans the original data also of the effects of small scale heterogeneities and geological noise (velocity inhomogeneities of dimension below the resolution power of the tomography), which remain in data after the B-type correction, and which are of course present in the original data. On the other hand, the B-type correction is weaker due to the fact that about 30 per cent of rays remain uncorrected and the models represent only lower limit estimate of anisotropy due to limited ray coverage of the volume. Generally speaking, while the gross features persist in all three types of inversions, the decrease of small-size velocity perturbations with depth is more pronounced in images with the corrections for anisotropy, particularly if the A-type correction is applied. All models are characterized by strong vertical smearing, which is a natural characteristic of teleseismic tomography (Figs 5 and 8).

Vertical cross-sections (Fig. 8) along the profile (see Fig. 1 for the location) running SSW–NNE though the SNSN array allows us to visualize more easily the differences in the well-resolved central part of the models. Amplitudes of the high-velocity heterogeneity in the NE end of the profile in the model produced with the original data (Fig. 8a), interpreted as a slab-like structure (Eken *et al.* 2007, 2008), decreases in the images from data corrected for anisotropy, particularly in cases with the A-type correction (Fig. 8b), which also eliminates small-scale heterogeneities (noise in a broader sense). Convergently, dipping high velocities in the lithosphere domains of the Central (yellow stations) and Northern Svecofennian (green stations) (Eken *et al.* 2010), are likely responsible for the

high-velocity heterogeneity occurred at depths of about 300 km and a distance of about 1000 km away from the southern edge of the profile. One of several of definitions of the LAB is associated with a seismic velocity decrease, though the boundary remains elusive, particularly in cratonic areas (Eaton *et al.* 2009). Keeping in mind limitations of any regional tomography as to velocity changes between layers, we can associate the depth to which lateral velocity variations extend as an approximation of the LAB. Applying this logic to Fig. 8b we observe a lithosphere thickening towards the central part of Fennoscandia and thinning toward the North (Plomerová & Babuška 2010). This behaviour is also detectable on several tested parallel profiles. A steep thinning of the lithosphere in the SW part of the cross-section, though in less resolved part of the model, correlates with the well-documented shape of the Fennoscandian keel as deduced from several studies using different methods and datasets, for example in body-wave tomography (Shomali *et al.* 2006), surface wave tomography (Cotte *et al.* 2002) or body-wave anisotropy (Plomerová *et al.* 2002). Priestley and Tilmann (2009) point out the limitations of regional body-wave tomographic models in mapping the lithosphere thickness because we essentially only determine wave-speed perturbations from an unknown horizontal average and not absolute velocities. Therefore, any feature which extends laterally across the whole region beneath a seismic network turns out to be invisible.

Though both types of data correction for mantle anisotropy are not perfect, resulting isotropic images (Figs 8b and c) show a significant decrease of amplitudes of perturbations bellow 250 km depth. The high-velocity perturbations dominate within the mantle lithosphere (Plomerová & Babuška 2010). The initially distinct high-velocity perturbations in the sub-lithospheric depths are weaker in images from data corrected for anisotropy and thus, it do not tempt to be interpreted as a subduction (Eken *et al.* 2008). We do not deny an existence of high-velocity perturbations deeper in the mantle at all, but stronger effects from heterogeneous and anisotropic shallower mantle should be considered. Some combinations of noise, both heterogeneous and anisotropic small-scale (tenths of kilometres) structures can seem to be even more important on the first glance. But large-scale anisotropic structures at scales of hundreds of kilometres do obscure the velocity images of sub-lithospheric mantle, though complete considering of anisotropic propagation or correcting for 3D anisotropy is not yet fully applicable.

6 DISCUSSION

Isotropic tomography studies in and around the Baltic Shield have suggested velocity perturbations of ∼+2–3 per cnet for *P* and *S* waves (Plomerová *et al.* 2001; Shomali *et al.* 2002, 2006; Sandoval *et al.* 2004; Bruneton *et al.* 2004; Eken *et al.* 2007, 2008, 2010). Standard resolution analyses imply that these studies show significant and resolved lateral variations in velocity to greater depths than appears to be consistent with our current understanding of the physical properties of mantle materials and our preconceptions about plausible variations in temperature and composition in the area. Moreover, several studies clearly demonstrate the existence of seismic anisotropy in the upper mantle beneath the Shield (Wylegalla *et al.* 1999; Plomerová *et al.* 2001, 2002, 2006; Babuška & Plomerová 2006; Pedersen *et al.* 2006; Vecsey *et al.* 2007; Eken *et al.* 2008, 2010).

The Shield possesses the characteristics of a continental lithosphere with a thick, undulated and sharply stepping lithospheric root—cratonic keel (Sandoval *et al.* 2004; Babuška & Plomerová 2006; Olsson 2007; Plomerová *et al.* 2002, 2008; Eken *et al.* 2007, 2008). Traditionally, a sub-lithospheric flow around this keel would be considered as an explanation for the mechanism of observed anisotropy (Wylegalla *et al.* 1999; Pedersen *et al.* 2006). In such a case, the fast shear-wave polarization directions and the high velocities retrieved from surface wave inversions would be parallel to the current plate motion and any regional variation would reflect deflections of the mantle flow (Bormann *et al.* 1996). However, the fast shear-wave polarization directions evaluated in central Fennoscandia (with the use of data from the SVEKALAPKO array and the SNSN) indicate distinct directional and geographical variations, which are not consistent with present day sub-lithospheric mantle flow around the Fennoscandian root (Plomerová *et al.* 2006, 2008; Vecsey *et al.* 2007; Eken *et al.* 2010). Due to the long history of the Precambrian lithosphere, which includes accretionary processes related to different phases of plate tectonics (Plomerová & Babuška 2010) one can expect complicated lithosphere–asthenosphere structures beneath regions which are now 'intra-plate' areas, including Fennoscandia (Plomerová *et al.* 2008).

Both lateral heterogeneities and anisotropy can produce similar patterns in the *P*-wave residuals and we are aware of trade-offs between the effects of heterogeneity and anisotropy. Moreover, anisotropy itself varies laterally and can be depth-dependent as well. However, the relatively simple patterns observed in the *P*-residual spheres, their similarity at many stations within individual regions, and the evident consistency between the shear wave splitting and *P*-residual data (Eken *et al.* 2010) allow us to consider simplified models (Fig. 3) of the mantle lithosphere formed by large-scale consistent anisotropy with inclined foliations (*a*,*c*) or plunging lineation *a* as a reasonable first approximation of the mantle lithosphere fabric. Moreover, with the use of these models we can separate to a large extent the effects of anisotropy and heterogeneities.

Joint inversions of anisotropic parameters estimated from body waves (SKS and *P*-wave analyses) indicate distinct domain-like anisotropic structures in the Fennoscandian mantle lithosphere (Plomerová *et al.* 2001, 2006; Vecsey *et al.* 2007; Eken *et al.* 2010). 3-D self-consistent anisotropic structures with plunging symmetry axes approximate fabrics below the SNSN (Eken *et al.* 2010) and thus support the idea that the laterally varying anisotropy observed beneath the shield, exhibiting a uniform fabric within sharply bounded domains, is largely of fossil character related to ancient large-scale processes (Plomerová & Babuška 2010). A detailed argumentation for locations of the observed anisotropy within the mantle lithosphere beneath the SNSN based on, for example, results of splitting of *Ps* converted waves at the 410 km discontinuity (Olsson 2007) and characteristics of directional variations of evaluated shear-wave splitting in a broader region, including southern Finland (SVEKALAPKO experiment, Vecsey *et al.* 2007) is published in Eken *et al.* (2010).

The presence of zones of different anisotropic character may distort images retrieved in isotropic inversions of teleseismic *P*-wave traveltimes. As a first step, we used the simplest possible approach to compensating for the effects of anisotropy on the inversions by presuming that deviations from the individual station directional *P*-mean residuals are caused by anisotropy. These deviations are removed from the travel time data (the A-type correction) before further processing and tomographic inversion. The resulting increase of the data variance reduction from 51 to 79 per cent is large, which is partly due to a reduction in the true number of degrees of freedom in the data, because small scale (crust) heterogeneities, which might be considered as noise, were probably greatly reduced

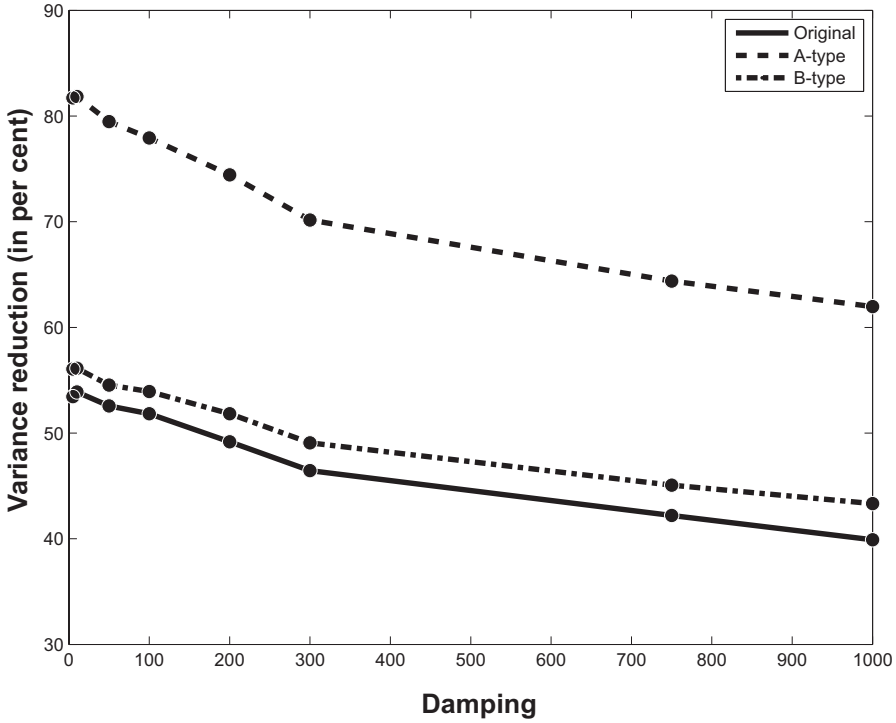

Figure 7. Variance reductions of the three velocity-perturbation models versus damping factor of inversions.

by the procedure. This implies that 'corrections' to compensate for crustal structure may be very important, as discussed by for example Kissling *et al.* (1997). On the other hand, Shomali *et al.* (2002) found that the inversion of TOR data from Southern Sweden, Denmark and North Germany was relatively insensitive to details of how the crustal structure was handled in the inversion.

Our current knowledge regarding mineral physics and the composition and temperature of the Shield mantle, implies that lateral velocity variations at depths of over 250 km and of the magnitude deduced in Eken *et al.* (2007) may be difficult to explain. The new inversions with data corrected for anisotropy (Figs. 6–8) could, therefore, be an indication that some lateral velocity variations (Figs 5 and 8a) are, perhaps in part, artifacts due to neglecting anisotropy in isotropic inversions.

To go further, we attempted to separate the components d_{aniso} and d_{bias} in the data. To do this we calculated synthetic contributions to the relative residuals according to anisotropic models (Fig. 3) retrieved by joint inversions of body-wave anisotropic parameters (the B-type corrections). Observations of anisotropic signatures indicate that anisotropy in the lithospheric mantle beneath the stations is fairly consistent in orientation and magnitude. The synthetic traveltime residuals vary only smoothly with azimuth and inclination. We associate more rapid variations over azimuth and inclination with lateral heterogeneity and/or with propagation within two bordering domains. Stations situated above such boundaries, exhibit usually 'no P pattern' and/or weak shear-wave anisotropy (e.g. Plomerová *et al.* 2001). In such cases, we do not correct the travel times of the station at all (e.g. SVA, OSK, BYX, UDD, and see Fig. 1) although travel times to the stations which are used as the input in velocity tomography are effected by anisotropic structures. This means that the B-type corrections for anisotropy are underestimated considering the whole array, which is reflected, for example in values of the radial rms (Fig. 6a).

Irrespective of the accuracy of the estimates of the anisotropic parameters, the resulting velocity perturbations are reasonable when compared with findings from mineral physics. The differences in the inverted models are therefore a strong indication that anisotropy can partly distort the *P*-wave tomographic image, and that the risk of bias due to the effects of seismic anisotropy should not be ignored. Ignoring the anisotropy with inclined symmetry axes smears the velocity perturbations to greater depths (Figs 5–8) and thus acts in a similar manner to smearing due to the ray geometry in the teleseismic tomography. The potential degradation of tomographic images may be more significantly in cases where remnant fabric produces laterally varying anisotropy, than if the anisotropy is homogeneous over the whole domain. Assuming the estimates of the effects of anisotropy are reliable, then the models with data corrected for anisotropy (Figs 5b and c) should produce more representative images of the Earth's upper mantle.

The relatively stable patterns observed in the directional variations of *P* traveltime residuals within the identified groups of stations (lithospheric mantle domains), along with the observed characteristics of shear-wave splitting (Eken *et al.* 2010), suggest that the *P* residuals, as a general input to isotropic tomography, do genuinely contain a significant signal related to anisotropy. The concept of using this information in order to correct the data for anisotropy and thus enhance reliability of images from isotropic tomographic inversions is promising. Dealing with large-scale velocity structure of the upper mantle, we need not take care of non-realistic small-scale perturbations mapped down to the mantle from small-scale heterogeneities mostly in the crust or from noise, eliminated in the A-type corrections. On the other hand, the B-type correction under-estimates effects of the large-scale anisotropy and does not enables to avoid mapping the small-scale heterogeneities into the mantle. To assess thoroughly the potential of the anisotropic correction method, conducting additional synthetic tests, including models

© 2011 The Authors, *GJI*, **188,** 600–612
Geophysical Journal International © 2011 RAS

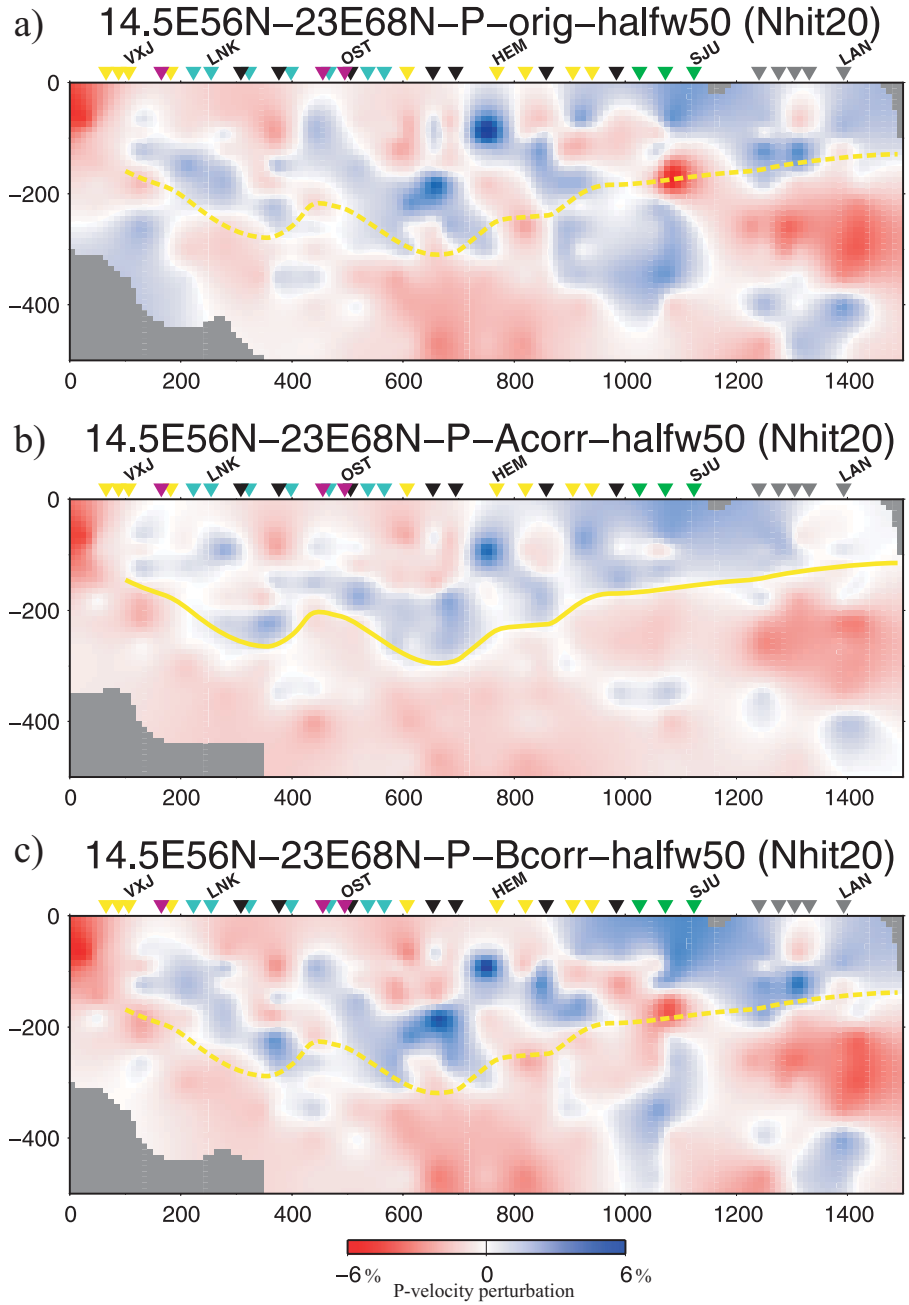

Figure 8. Cross-sections through the velocity perturbation models along the SW–NE profile (for location see Fig. 1) derived from data with (a) no correction for anisotropy (original data), (b) with the A-type and (c) the B-type corrections for anisotropy. The perturbations represent a 100 km wide band along the profile. Stations coloured according to their *P*-pattern lie in a band of the doubled width along the profile, as they affect the perturbations in deeper parts of the models. The yellow curve in (b) could be considered as a rough approximation of the lithosphere–asthenosphere boundary. The same boundary but dashed is superimposed with velocity-perturbations images in (a) and (c) and is added to emphasize the differences between the high-velocity perturbations at sub-lithospheric levels in the cross-sections.

with laterally varying zones of anisotropy and even depth-dependent anisotropic characteristics will be helpful.

7 CONCLUSIONS

General features of tomographic images of the original and the anisotropy corrected (A- and B-type) data are similar. Radial rms and cross-correlation analyses of the resulting perturbations show that most of the differences between the models occur within the upper ∼250 km of the upper mantle. A clear characteristic of the new inversions is a decrease of amplitudes of the velocity perturbations below ∼200 km depth in the images calculated from data corrected for anisotropy. The high-velocity heterogeneity between 65° and 68°N at depths below ∼250 km, interpreted in the original tomography (less well-resolved region) as ‘a slab-like’ structure, almost vanish in the images after corrections for anisotropy and represent the major difference between the velocity perturbation images from the original and the anisotropy corrected data. Other observed differences are relatively small except in marginal, less resolved nodes.

An increase of data variance reduction up to 79 per cent in the case of the A-type correction, which is considered to eliminate both effects related to anisotropy and small-scale heterogeneities, indicates that the model does reflect well the large-scale upper mantle structures, which are our primary target in these studies. Moreover, regardless of the robustness of the corrections for anisotropy, the magnitude of retrieved velocity perturbations (up to $\sim\pm3$ per cent) is in accord with findings of mineral physics.

Models of backazimuth variations of *P*-wave polarizations (P_{pol}) support the existence of anisotropic structures with dipping axes of symmetry rather than isotropic models with dipping interfaces. This represents independent support for the anisotropic models of the mantle lithosphere retrieved by joint inversions of body-wave anisotropic parameters (*P*-residual spheres and shear-wave splitting).

Ignoring effects of large-scale anisotropy related to the fabrics of the mantle lithosphere beneath the Baltic Shield can contaminate large-scale tomographic images, particularly at depths below ~200 km and in less resolved regions. Such effects should be taken into consideration in future high-resolution velocity-perturbation studies of the continental upper mantle in provinces with geographically varying anisotropic structure.

ACKNOWLEDGMENTS

Financial support of the Grant Agency of Academy of Sciences of the Czech Republic (Grant No: IAA300120709) is acknowledged. The authors thank Andrew Frederiksen for providing the RAYSUM code used for the calculations of synthetic waveforms and Toivo Korja for providing the Moho depths beneath the region. We are grateful G. Laske, B. Romanowicz and an anonymous referee for suggestions and recommendations that have helped us to improve the ms. substantially.

REFERENCES

Aki, K. & Kaminuma, K., 1963. Phase velocity of Love waves in Japan, Part 1, Love waves from Aletutian shock of March 9, 1957, *Bull. Earthq. Res. Inst.,* **41,** 243–259.

Aki, K. & Lee, W.H.K., 1976. Determination of three-dimensional velocity anomalies under a seismic array using first P arrival times from local earthquakes. 1. A homogeneous initial model, *J. geophys. Res.,* **81,** 4381–4399.

Aki, K., Christoffersson, A. & Husebye, E., 1977. Determination of the three-dimensional seismic structure of the lithosphere, *J. geophys. Res.,* **82,** 277–296.

Anderson, D.L., 1961. Elastic wave propagation in layered anisotropic media, *J. geophys. Res.,* **82,** 277–296.

Anderson, D.L. & Dziewonski, A.M., 1982. Upper mantle anisotropy: Evidence from free oscillations, *Geophys. J. R. astr. Soc.,* **69,** 383–404.

Ando, M., Ishikawa, Y. & Wada, H., 1980. *S*-wave anisotropy in the upper mantle under a volcanic area in Japan, *Nature,* **286,** 43–46.

Babuška, V., Plomerová, J. & Šílený, J., 1984. Spatial variations of Presiduals and deep-structure of the European lithosphere, *Geophys. J. R. astr. Soc.,* **79,** 363–383.

Babuška, V. & Cara, M., 1991. *Seismic Anisotropy in the Earth*, Kluwer Academic Publishers, Dordrecht.

Babuška, V. & Plomerová, J., 2006. European mantle lithosphere assembled from rigid microplates with inherited seismic anisotropy, *Phys. Earth. planet. Inter.* **158,** 264–280.

Ben Ismail, W. & Mainprice, D., 1998. An olivine fabric database: An overview of upper mantle fabrics and seismic anisotropy, *Tectonophysics* **296,** 145–157.

Bird, P., 2003. An updated digital model of plate boundaries, *Geochem. Geophys. Geosyst.,* **4**(3), 1027, doi:10.1029/2001GC000252.

Bormann, P., Grünthal, G., Kind, R. & Montag, H., 1996. Upper mantle anisotropy beneath central Europe from SKS wave splitting: effects of absolute plate motion and lithosphere–asthenosphere boundary topography?, *J. Geodyn.* **22,** 11–32.

Bödvarsson, R., 1999. The new Swedish Seismic Network, *ORFEUS Newsletter*, Vol. 1, no 3.

Bruneton, M., Pedersen, H.A., Farra, V., Arndt, N.T., Vacher, P. & SVEKALAPKO Seismic Tomography Working Group, 2004. Complex lithospheric structure under the central Baltic Shield from surface wave tomography, *J. geophys. Res.,* **109,** B10303.

Cotte, N., Pedersen, H.A. & TOR Working Group, 2002. Sharp contrast in lithospheric structure across the Sorgenfrei–Tornquist Zone as inferred by Rayleigh wave analysis of TOR1 project data, *Tectonophysics,* **360,** 75–88.

Eberhart-Phillips, D. & Henderson, C.M., 2004. Including anisotropy in 3-D velocity inversion and application to Marlborough, New Zealand, *Geophys. J. Int.* **156** (2), 237–254.

Eaton, D.W., Darbyshire, F., Evans, R.L., Grutter, H., Jones, A.G. & Yuan, X., 2009. The elusive lithosphere-asthenosphere boundary (LAB) beneath cratons, *Lithos*, **109,** 1–22.

Eken, T., Shomali, H., Roberts, R. & Bödvarsson, R., 2007. Upper mantle structure of the Baltic Shield below the Swedish National Seismological Network (SNSN) resolved by teleseismic tomography, *Geophys. J. Int.,* **169,** 617–630.

Eken, T., Shomali, Z.H., Roberts, R., Hieronymus, Ch.F & Bodvarsson, R., 2008. S and P velocity heterogeneities within the upper mantle below the Baltic Shield, *Tectonophysics*, **462,** 109–124.

Eken, T., Plomerová, J. Roberts, R. Vecsey, L. Babuška, V., Shomali, H. & Bodvarsson, R., 2010. Seismic anisotropy of the mantle lithosphere beneath the Swedish National Seismological Network (SNSN), *Tectonophysics,* **480,** 241–258.

Evans, J. & Achauer, U., 1993. Teleseismic velocity tomography using the ACH method: Theory and application to continental-scale studies, in *Seismic Tomography: Theory and Practice,* pp. 319–360, eds Iyer, H.M. & Hirahara, K., Chapman & Hall, London.

Fontaine, F.R., Barruol, G., Kennett, B., Bokelmann, G. & Reymond, D., 2009. Upper mantle anisotropy beneath Australia and Tahiti from P wave polarization: Implications for real-time earthquake location, *J. geophys. Res.,* **114,** B03306, doi:10.1029/2008JB005709.

Frederiksen, A.W. & Bostock, M.G., 2000. Modelling teleseismic waves in dipping anisotropic structures, *Geophys. J. Int.,* **141,** 401–412.

Fouch, M.J. & Rondenay, S., 2006. Seismic anisotropy beneath stable continental interiors, *Phys. Earth planet. Int.*, **158,** 292–320.

Gresillaud, A. & Cara, M., 1996. Anisotropy and *P*-wave tomography: A new approach for inverting teleseismic data from a dense array of stations, *Geophys. J. Int.,* **126,** 77–91.

Hearn, T.M., 1999. Uppermost mantle velocities and anisotropy beneath Europe, *J. geophys. Res.,* **104,** 15123–15139.

Hirahara, K. & Ishikawa, Y., 1984. Travel time inversion for 3-D *P*-wave velocity anisotropy, *J. Phys. Earth,* **32,** 197–218.

Ishise, M. & Oda, H., 2008. Subduction of the Philippine Sea slab in view of *P*-wave anisotropy, *Phys. Earth planet. Inter.,* **166,** 83–96.

Kennett, B. & Engdahl, R. 1991. Travel times for global earthquake location and phase identification, *Geophys. J. Int.*, **105,** 429–465.

Kissling, E., Ansorge, J. & Baumann, M. 1997. Methodological considerations of 3D crustal modelling by 2D seismic methods, in *Deep structure of the Swiss Alps,* pp. 31–38. eds, Heitzamann, P., Lehner, P., Mueller, St., Pfiffner, A. & Steck, A., Birkhäuser, Basel.

Korsman, K., Korja, T., Pajunen, M., Virransalo, P. & the GGT/SVEKA Working Group, 1999. The GGT/SVEKA transect—structure and evolution of the continental crust in the Palaeoproterozoic Svecofennian Orogen in Finland, *Int. Geol. Rev.,* **41,** 287–333.

Levin, V., Menke, W. & Park, J., 1999. Shear wave splitting in Appalachians and Urals: a case for multilayer anisotropy, *J. geophys. Res.* **104,** 17975–17994.

Levin, V., Roecker, S., Graham, P. & Hosseini, A., 2008. Seismic anisotropy indicators in western Tibet: Shear wave splitting and receiver function analysis, *Tectonophysics*, **462,** 99–108.

Lloyd, S.M. & van der Lee, S., 2008. Influence of observed mantle anisotropy on isotropic tomographic models, *Geochem. Geophys. Geosyst.,* **9**, Q07007, doi:10.1029/2008GC001997.

Mainprice, D. & Silver, P.G., 1993. Interpretation of SKS-waves using samples from the subcontinental lithosphere, *Phys. Earth. planet. Inter.*, **78,** pp. 257–280.

Menke, W., 1989. *Geophysical Data Analysis: Discrete Inverse Theory,* International Geophysics Series, Vol. 45, Academic Press, London, 289pp.

Montagner, J.-P., 1998. Where can seismic anisotropy be detected in the Earth's mantle? In boundary layers, *Pure appl. Geophys.,* **151,** 223–256.

Nolet, G., 1987. Seismic wave propagation and seismic tomography, *Seismic Tomography*, pp. 1–23, ed. Nolet, G., Reidel, Dordrecht.

Oliver, J. & Murphy, l. 1971. WWNSS: Seismology's global network of observing stations, *Science,* **174,** 254–262.

Olsson, S., 2007. Analyses of seismic wave conversion in the crust and upper mantle beneath the Baltic Shield, *PhD thesis*, Uppsala Univ.

Pedersen, H.A., Bruneton, M., Maupin, V. & SVEKALAPKO STWG, 2006. Lithospheric and sublithospheric anisotropy beneath the Baltic Shield from surface wave array analysis, *Earth planet. Sci. Lett.,* **244,** 590–605.

Plomerová, J., Šílený, J. & Babuška, V., 1996. Joint interpretation of upper mantle anisotropy based on teleseismic P-travel time delays and inversion of shear-wave splitting parameters, *Phys. Earth planet. Int.,* **95,** 293–309.

Plomerová, J., Arvidsson, R., Babuška, V., Granet, M., Kulhánek, O., Poupinet, G. & Šílený, J., 2001. An array study of lithospheric structure across the Protogine Zone, Varmland, south-central Sweden—signs of a paleocontinental collision, *Tectonophysics,* **332,** 1–21.

Plomerová, J., Babuška, V., Vecsey, L., Kouba, D. & TOR Working Group, 2002. Seismic anisotropy of the lithosphere around the Trans-European Suture Zone (TESZ) based on teleseismic body-wave data of the Tor experiment, *Tectonophysics,* **360,** 89–114.

Plomerová, J., Babuška, V., Vecsey, L., Kozlovskaya, E., Raita, T. & SSTWG, 2006. Proterozoic–Archean boundary in the upper mantle of eastern Fennoscandia as seen by seismic anisotropy, *J. Geodyn,* **41,** 400–410, doi:10.1016/j.jog.2005.10.008.

Plomerová, J., Frederiksen, A.W. & Park, J., 2008. Seismic anisotropy and geodynamics of the lithosphere-asthenosphere system, *Tectonophysics,* **462,** 1–6.

Plomerová, J. & Babuška, V., 2010. Long memory of mantle lithosphere fabric-European LAB constrained from seismic anisotropy, *Lithos,* **120,** 131–143, doi:10.1016/j.lithos.2010.01.008.

Pristley, K. & Tilmann, F., 2009. Relationship between the upper mantle high velocity seismic lid and the continental lithosphere, *Lithos,* **109,** 112–124.

Rawlinson, N., Pozgay, S. & Fishwick, S., 2010. Seismic tomography: A window into deep Earth, *Phys. Earth planet. Int.,* **178,** 101–135.

Savage, M.K., 1999. Seismic anisotropy and mantle deformation: what have we learned from shear wave splitting?, *Rev. Geophys.,* **37,** 65–106.

Sandoval, S., Kissling, E., Ansorge, J. & the SVEKALAPKO Seismic Tomography Working Group, 2004. High-resolution body wave tomography beneath the SVEKALAPKO array – II. Anomalous upper mantle structure beneath the central Baltic Shield, *Geophys. J. Int.,* **157,** 200–214.

Schulte-Pelkum, V., Masters, G. & Shearer, P.M., 2001. Upper mantle anisotropy from long-period P polarization, *J. geophys. Res.,* **154,** 166–178.

Shomali, Z.H., Roberts, R.G. & the TOR Working Group, 2002. Non-linear body wave teleseismic tomography along the TOR array, *Geophys. J. Int.,* **148,** 562–575.

Shomali, Z.H., Roberts, R.G., Pedersen, L.B. & the TOR Working Group, 2006. Lithospheric structure of the Tornquist Zone resolved by nonlinear P and S teleseismic tomography along the TOR array, *Tectonophysics,* **416**(1–4): 133–149.

Šílený, J. & Plomerová, J., 1996. Inversion of shear-wave splitting parameters to retrieve three-dimensional orientation of anisotropy in continental lithosphere, *Phys. Earth planet. Int.,* **95,** 277–292.

Silver, P.G. & Chan, W.W., 1988. Implications for continental structure and evolution from seismic anisotropy, *Nature,* **335,** 34–39.

Sobolev, S., Gresillaud, A. & Cara, M., 1999. How robust is isotropic delay time tomography for anisotropic mantle?, *Geophys. Res. Lett.,* **26**(4), 509–512.

Thurber, C. & Ritsema, J., 2007. Theory and observations—seismic tomography and inverse methods, in, *Seismology and the Structure of the Earth, Treatise on Geophysics,* Vol. 1, pp. 323–360, ed. Schubert, G., Elsevier, Oxford.

Vecsey, L., Plomerová, J., Kozlovskaya, E. & Babuška, V., 2007. Shear-wave splitting as a diagnostic of varying upper mantle structure beneath south-eastern Fennoscandia, *Tectonophysics,* **438,** 57–77, doi:10.1016/j.tecto.2007.02.017.

Vinnik, L.P., Kosarev, G. & Makeeva, L., 1984. Lithosphere anisotropy from the observation of SKS and SKKS waves, *Doklady Akad. Nauk., USSR* **278**(6), 1335–1339.

Wylegalla, K., Bock, G., Gossler, J., Hanka, W. & TOR Working Group, 1999. Anisotropy across the Sorgenfrei–Tornquist Zone from shear wave splitting, *Tectonophysics,* **314,** 335–350.